

Magnetic ordering and spin dynamics in the $S = \frac{5}{2}$ staggered triangular lattice antiferromagnet $\text{Ba}_2\text{MnTeO}_6$

Lisi Li,¹ Narendrakumar Narayanan,^{2,3} Shangjian Jin,¹ Jia Yu,¹ Zengjia Liu,¹ Hualei Sun,¹ Chin-Wei Wang,^{1,2} Vanessa K. Peterson,² Yun Liu,³ Sergey Danilkin,² Dao-Xin Yao,¹ Dehong Yu,² and Meng Wang^{1,*}

¹Center for Neutron Science and Technology, School of Physics, Sun Yat-Sen University, Guangzhou, 510275, China

²Australian Nuclear Science and Technology Organisation, Lucas Heights NSW 2234, Australia

³Research School of Chemistry, The Australian National University, Canberra ACT 2601, Australia



(Received 5 June 2020; revised 22 August 2020; accepted 24 August 2020; published 9 September 2020)

We report studies of the magnetic properties of a staggered stacked triangular lattice $\text{Ba}_2\text{MnTeO}_6$ using magnetic susceptibility, specific heat, neutron powder diffraction, inelastic neutron scattering measurements, and first-principles density functional theory calculations. Neutron diffraction measurements reveal $\text{Ba}_2\text{MnTeO}_6$ to be antiferromagnetically ordered with a propagation vector $\mathbf{k} = (0.5, 0.5, 0)$ and Néel transition temperature of $T_N \approx 20$ K. The dominant interaction derived from the Curie-Weiss fitting to the inverse DC susceptibility is antiferromagnetic. Modeling of the inelastic neutron scattering data with linear spin wave theory yielded magnetic exchange interactions for the nearest intralayer, nearest interlayer, and next-nearest interlayer of $J_1 = 0.27(3)$, meV $J_2 = 0.27(3)$ meV, and $J_3 = -0.05(1)$ meV, respectively, and a small value of easy-axis anisotropy of $D_{zz} = -0.01$ meV. We derive a magnetic phase diagram that reveals a collinear stripe-type antiferromagnetic order that is stabilized by the competition between J_1 , J_2 , and J_3 .

DOI: [10.1103/PhysRevB.102.094413](https://doi.org/10.1103/PhysRevB.102.094413)

I. INTRODUCTION

Geometrically frustrated magnets have attracted attention due to their novel low temperature states, such as spin ice, spin liquid, and noncollinear magnetic states [1–4]. The triangular lattice is a representative geometrically frustrated structure, and although simple, exhibits a diversity of ground states [5,6]. For a two-dimensional Heisenberg triangular lattice antiferromagnet with dominant nearest-neighbor (NN) intralayer coupling, a ground state with a 120° spin structure within the plane is realized, such as in $\text{Ba}_8\text{MnNb}_6\text{O}_{24}$ [7], $\text{Rb}_4\text{Mn}(\text{MoO}_4)_3$ [8], $\text{Ba}_3\text{MnSb}_2\text{O}_9$ [9], and $\text{Ba}_2\text{La}_2\text{MTe}_2\text{O}_{12}$ ($M = \text{Co}, \text{Ni}$) [10,11]. When anisotropy and further-neighbor magnetic coupling arise, the ordered state that finally occurs is a consequence of a subtle balance among these factors [12]. In CuCrO_2 , an incommensurate magnetic structure is stabilized by a combination of the coupling between adjacent planes, the anisotropic in-plane NN interlayer interactions, and the weak antiferromagnetic (AF) next-nearest-neighbor (NNN) interaction [13–15]. In CuFeO_2 , a three-dimensional collinear magnetic structure forms which is stabilized by the strong third-neighbor intralayer coupling and an interlayer coupling [16,17]. Strong easy axis anisotropy also plays an important role in determining the magnetic ground state, such as in 2H-AgNiO_2 , which displays a collinear alternating stripe-type magnetic structure [18–20]. Therefore the triangular lattice provides a playground for exploring exotic magnetic ground states.

In $\text{Ba}_2\text{MnTeO}_6$, Mn^{2+} ions form a uniform triangular layer in the ab plane and stack along the c axis [21]. The triangular

lattice shifts to the center of the triangle of the neighboring triangular lattice viewed along the c axis as shown in Fig. 1(b). As a result, the triangular layers are stacked as $ABCABC \dots$ along the c axis as shown in Fig. 1(a), where A , B , and C are the Mn(1), Mn(2), and Mn(3) layers, respectively. The structure is similar to $\text{Ba}_2\text{CoTeO}_6$, with two inequivalent Co sites in $\text{Ba}_2\text{CoTeO}_6$, $\text{Co}^{2+}(1)$ and $\text{Co}^{2+}(2)$, with different octahedral environments. $\text{Co}^{2+}(1)$ ions form a triangular lattice and $\text{Co}^{2+}(2)$ ions form a bilayer triangular lattice [22–24]. In $\text{Ba}_2\text{MnTeO}_6$, there is only one inequivalent Mn site in the crystal structure. The nearest intralayer Mn-Mn distance [5.7533(6) Å] is almost the same as the nearest interlayer distance [5.7566(6) Å]. In the staggered stacked triangular lattice, the stacking geometry is characterized by the ratio of the nearest interlayer distance of neighboring layers to that of the intralayer distance, and critically influences magnetic properties [25]. For example, the ratio in two-dimensional NiGa_2S_4 is 3.31 [26–28] and, in the triangular arrangement of the spin chain CsNiCl_3 , is 0.41 [29–32]. The ratio in $\text{Ba}_2\text{MnTeO}_6$ is close to 1. This motivated us to explore exotic properties in this highly geometrically frustrated compound and to compare them with two-dimensional layer and one-dimensional spin chain systems. To our knowledge, no detailed experimental investigation has been conducted to explore the magnetic properties of $\text{Ba}_2\text{MnTeO}_6$. Therefore an experimental investigation into the role of the interlayer and intralayer couplings on magnetic properties in this material is of great importance.

In this paper, we investigate the magnetic properties of $\text{Ba}_2\text{MnTeO}_6$ by combining magnetic susceptibility, specific heat, neutron powder diffraction (NPD), and inelastic neutron scattering (INS) measurements with density functional theory (DFT) calculations. We find that $\text{Ba}_2\text{MnTeO}_6$ exhibits a

*wangmeng5@mail.sysu.edu.cn

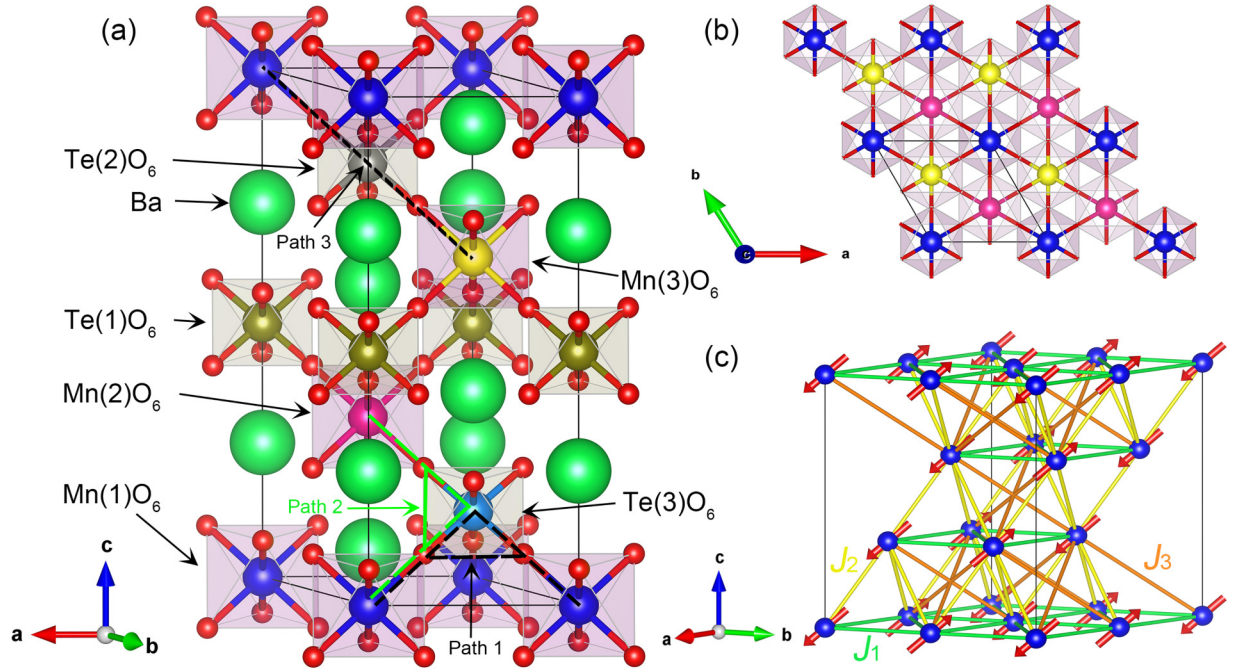


FIG. 1. (a) Unit cell of Ba₂MnTeO₆. Dashed curves show the superexchange coupling paths of Mn²⁺-O²⁻-O²⁻-Mn²⁺ and Mn²⁺-O²⁻-Te⁶⁺-O²⁻-Mn²⁺ for the nearest intralayer (path 1) and interlayer (path 2), and the next-nearest interlayer (path 3) coupling with path of Mn²⁺-O²⁻-Te⁶⁺-O²⁻-Mn²⁺. (b) Layer structure of the MnO₆ octahedron viewed along the *c* axis. (c) Sketch of the magnetic structure of Ba₂MnTeO₆. An exchange coupling network for J_1 , J_2 , and J_3 is shown as the chemical bonds of pairs of Mn²⁺ ions in green, yellow, and orange, respectively.

three-dimensional stripe-type collinear AF order with a propagation vector of $\mathbf{k} = (0.5, 0.5, 0)$ below the magnetic phase transition temperature of $T_N \approx 20$ K. Modeling of the INS data reveals a ferromagnetic (FM) NNN interlayer coupling J_3 in addition to the NN intralayer J_1 and NN interlayer J_2 couplings. Moreover, a small easy axis anisotropy D_{zz} is found, originating from a strong dipolar interaction that typically presents in large spin systems. We discuss the effect of these exchange couplings on the stabilization of the magnetic ground state of Ba₂MnTeO₆.

II. EXPERIMENT AND CALCULATION DETAILS

High-quality powder samples of Ba₂MnTeO₆ were synthesized by a conventional solid-state reaction. Stoichiometric starting materials BaCO₃ (99.99%), MnCO₃ (99%), and TeO₂ (99.99%) were ground thoroughly in an agate mortar and then pressed into a pellet. The pellet was calcined in air at 1150 °C for 6 days with several intermediate grindings to obtain a highly homogeneous powder. No impurity phase was detected in x-ray diffraction (XRD) data. However, ~ 1 wt.% of the impurity phase Mn₃O₄ was identified in NPD data [33]. Zero field cooled (ZFC) and field cooled (FC) magnetic susceptibility and specific heat measurements were performed using a physical property measurement system (PPMS, Quantum Design).

NPD experiments were conducted on the high intensity powder diffractometer Wombat installed at the OPAL reactor, ANSTO [34]. Data were collected from 3.8 to 70 K with a neutron wavelength of $\lambda = 2.4124$ Å. Powder samples were loaded into a cylindrical vanadium can with an aluminum cap.

NPD data were analyzed by employing the Rietveld method using the FULLPROF Suite software [35,36].

INS experiments were performed on the cold-neutron time-of-flight spectrometer Pelican at the OPAL reactor, ANSTO [37]. Incident neutron energies were $E_i = 3.7$ and 14.8 meV with corresponding energy resolution of $\Delta E = 0.14$ and 0.35 meV, respectively, determined by the full width at half maximum of the elastic peak from a standard vanadium sample. Powder samples were loaded into a cylindrical aluminum can and measured at 1.5 K. The background from an empty aluminum can was measured and subtracted from the data for the sample. Data analysis was performed using the program LAMP [38]. Linear spin wave theory was employed to model the INS data using the SPINW software[39].

DFT calculations were performed using full-potential linearized augmented plane-wave and local orbital method as implemented in the WIEN2K code [40]. The value of $R_{MT}K_{max}$ was set to 6. The mesh of special k points was selected to be $2 \times 2 \times 2$. Calculations were performed using a supercell (magnetic unit cell) containing 120 ions including 12 independent Mn²⁺ ions. The crystal structure parameters and AF structure were obtained from the NPD data. The density of states was calculated using the local spin density state (LSDA) [41] and LSDA+ U (FLL)+ J [42]. A coulomb repulsion U was added in the fully localized limit (FLL) and J considering the exchange hole contribution. Spin-orbital coupling (SOC) was included alongside the valence states in a second variational step with the scalar relativistic orbital obtained from the first variational step as the basis. The magnetic dipole-dipole interaction (MDDI) tensor was calculated using the code MCPHASE [43]. For the 12 Mn²⁺ ions in the magnetic

TABLE I. Fractional atomic coordinates, Wyckoff sites, and selected bond paths and bond angles of Ba₂MnTeO₆ at 70K determined by neutron powder diffraction. Refined profile factors are $R_p = 9.47\%$, $R_{wp} = 9.28\%$, and $\chi^2 = 2.94$. All crystallographic sites are fully occupied. The numbers in the brackets indicate errors.

Ions	Wyckoff site	x/a	y/b	z/c
Mn ²⁺	6c	0.0000	0.0000	0.0000
Ba ²⁺	3a	0.0000	0.0000	0.2640(14)
Te ⁴⁺	3b	0.0000	0.0000	0.5000
O ²⁻	18h	-0.1758(8)	-0.3516(16)	-0.0906(9)
Bond path	Lengths (Å)	Bond angle		Angles (deg)
Mn(1)-Mn(1) (J_1)	5.7533(6)	Mn(1)-O-Te(3)		178.1(7)
Mn(1)-Mn(2) (J_2)	5.7566(6)	O(4)-Te(3)-O(6) (path 1)		91.4(5)
Mn(1)-Mn(2) (J_3)	8.1387(7)	O(4)-Te(3)-O(17) (path 2)		88.6(5)

unit cell, contributions from Mn neighbors up to 20 Å were considered. The MDDI energies for different magnetic moment orientations were calculated by solving an eigenvalue problem as shown in Ref. [44].

III. CRYSTAL AND MAGNETIC STRUCTURE

A previous x-ray diffraction (XRD) study on Ba₂MnTeO₆ single crystals revealed a layered triangular lattice with trigonal symmetry in the space group $R\bar{3}m$ (No. 166) [21]. This structure was refined against the 70-K NPD data. Approximately 1 wt.% of the impurity phase Mn₃O₄ was identified in the NPD data and included in the refinement model shown in Fig. 2(a). Ba₂MnTeO₆ lattice parameters were determined to be $a = b = 5.7534(4)$ Å, $c = 14.1052(2)$ Å, $\alpha = \beta = 90^\circ$, and $\gamma = 120^\circ$. Details of the atom coordinates and some selected bond distances and bond angles are shown in Table I. NPD data could be described equally well using a Ba₂MnTeO₆ phase with the cubic space group $Fm\bar{3}m$. The positions of the Ba and O atoms in the $R\bar{3}m$ space group structure are slightly distorted compared to the $Fm\bar{3}m$ space group structure, and the two structures were unable to be distinguished using the NPD data [45]. Calculated Goldschmidt tolerance factors for Ba₂MnTeO₆ were $t \approx 1.013 > 1$, suggesting that the correct space group is $R\bar{3}m$ [46]. For Ba₂CoTeO₆ and Ba₂NiTeO₆, this factor was $t = 1.034$ and 1.048 , respectively. The suggested trigonal structures support those previously determined [22,47].

The magnetic order of the material was investigated using NPD at 3.8 K. Clear magnetic peaks appear in the neutron diffraction data in Fig. 2(b). A plot of the magnetic peak intensities against temperature reveals a Néel temperature of $T_N \approx 20$ K in Fig. 2(c). To determine the magnetic structure, NPD data at 3.8 K were indexed to a hexagonal unit cell. All magnetic peaks could be indexed with a propagation vector of $\mathbf{k} = (0.5, 0.5, 0)$. Magnetic peaks at $2\theta = 17.0^\circ$, 24.1° , 38.6° , and 42.5° correspond to $(H, K, L) = (0.5, -0.5, 1)$, $(0.5, 0.5, 0)$, $(0.5, 0.5, 3)$, and $(0.5, -0.5, 4)$, respectively. Here, the momentum transfer $|Q|$ is calculated from Miller indices (H, K, L) using the relation $|Q| = 2\pi\sqrt{4/3(H^2 + HK + K^2)/a^2 + L^2/c^2}$ in the $R\bar{3}m$ space group, where a and c are the lattice parameters.

Further, we performed Rietveld refinement of the structure based on representational analysis using the program BasIreps within the FULLPROF package [35,48,49]. The representational

analysis for the propagation vector $\mathbf{k} = (0.5, 0.5, 0)$ and space group $R\bar{3}m$ gives two nonzero irreducible representations (IR) for one magnetic site of Mn(0, 0, 0).

$$\Gamma_{\text{mag}}^{\text{Mn}} = \Gamma_1^1 + \Gamma_2^1 \quad (1)$$

The basis vector of the two IRs of Mn is shown in Table II. The magnetic structure was assumed to be described by a single IR, one of two basis vectors: (i) ψ_1 and (ii) the linear combination of ψ_2 and ψ_3 . We performed Rietveld refinement of these two IRs against our data, with IR Γ_2^1 having the better agreement of $R_{\text{mag}} = 5.49\%$ with a moment direction tilted from the ab plane at an angle of about 41° . From the NPD data, we could not conclusively determine the magnetic structure, given the closeness of the two magnetic R factors. We note that a magnetic structure with c component is more favorable in a layer structure with considerable interlayer coupling, such as in CuCrO₂ [14].

Figure 2(b) displays the observed and calculated NPD data at 3.8 K using the IR Γ_2^1 with profile factors of $R_p = 10.7\%$, $R_{wp} = 10.4\%$, $R_e = 5.43\%$, and $\chi^2 = 3.67$ along with the impurity phase Mn₃O₄. The magnetic moment of Mn²⁺ with a c axis component and tilting at an angle of 41° from the ab plane is determined to be $4.49(5)\mu_B$, which is close to the full moment of $5\mu_B$ in the high spin state of $S = 5/2$. The reduction of the moment could be attributed to hybridization and geometrical frustration as shown in Fig. 1(c).

Investigation of the magnetic anisotropy may lead to resolving the magnetic structure. Magnetic anisotropy could be determined using the MDDI and SOC [44,50]. Ideally, for Mn²⁺ in the high spin state $S = 5/2$, the residual SOC should be weak and the MDDI is maximum for electrons in the outer d orbitals in Ba₂MnTeO₆ [51]. We model the MDDI and SOC

TABLE II. The irreducible representations and corresponding basis vectors for the space group $R\bar{3}m$ with $\mathbf{k} = (0.5, 0.5, 0)$ and Mn coordination (0, 0, 0) and the corresponding refined magnetic profile factors R_{mag} .

IR	BV	Mn	R_{mag}
		$[m_a, m_b, m_c]$	
Γ_1^1	ψ_1	[1, 1, 0]	6.54%
Γ_2^1	ψ_2	[1, -1, 0]	5.49%
	ψ_3	[0, 0, 1]	

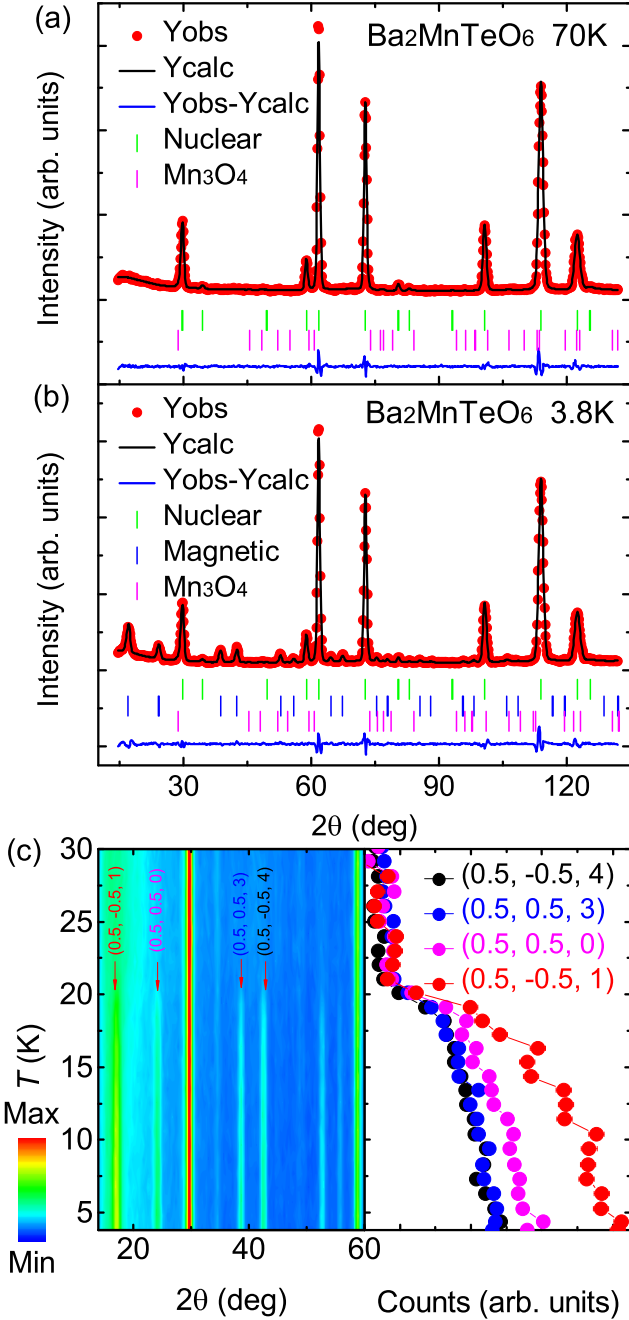


FIG. 2. Calculated and observed neutron diffraction data for $\text{Ba}_2\text{MnTeO}_6$ measured at (a) 70 and (b) 3.8 K. (c) Left: temperature dependence of NPD data in the range of 3.8 to 30 K measured with a step of 1 K. Right: temperature dependence of the integrated intensities of magnetic peaks at $(0.5, -0.5, 1)$, $(0.5, 0.5, 0)$, $(0.5, 0.5, 3)$, and $(0.5, -0.5, 4)$.

energy as described in the experimental section for a tilting (θ) of the magnetic moments from the $[-1, 1, 0]$ direction on the ab plane towards the c axis. Both the relative MDDI energy ΔE_{RMDD} and SOC energy ΔE_{SOC} exhibit a minimum around 55° from the ab plane and therefore the total anisotropy energy also has a minimum around 55° , is in good agreement with the experimental result of 41° as shown in Fig. 3. Thus anisotropy of $\text{Ba}_2\text{MnTeO}_6$ is dominated by MDDI but with a small

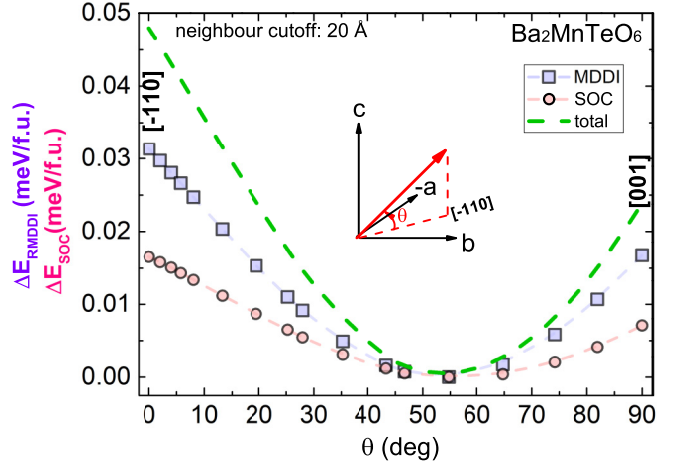


FIG. 3. Relative MDDI and SOC energies for different angles of the Mn^{2+} magnetic moments tilting from $[-1, 1, 0]$ towards the c axis. The energy minimum is around 55° .

contribution from SOC. Therefore we determine the magnetic structure to be collinear stripe-type AF order corresponding to the IR Γ_2^+ . Neutron diffraction measurements on a single crystal sample are needed to confirm the magnetic structure.

IV. MAGNETIC SUSCEPTIBILITY

Figure 4(a) shows the temperature dependence of zero field cooling (ZFC) and field cooling (FC) DC susceptibility $\chi(T)$ data of $\text{Ba}_2\text{MnTeO}_6$ measured with a magnetic field of $\mu_0 H = 0.1$ T. Divergence of the ZFC and FC susceptibility at ~ 41 K could be attributed to the impurity phase Mn_3O_4 , which orders ferrimagnetically below this temperature [52,53]. The susceptibility measured at low magnetic field is sensitive to the ferrimagnetic signal of the Mn_3O_4 impurity, which has been reported in other Mn^{2+} containing compounds such as Mn_2OBO_3 [54], $\text{Sr}_2\text{MnTeO}_6$ [55], and $\text{Mn}_4\text{Ta}_2\text{O}_9$ [50]. Near 20 K, a small kink appears in the ZFC and FC data which arises from the intrinsic AF transition of $\text{Ba}_2\text{MnTeO}_6$, consistent with the NPD data. For the higher magnetic fields of $\mu_0 H = 1$ and 5 T as shown in Fig. 4(b), the divergence at ~ 41 K is weakened, while the intrinsic magnetic transition at 20 K could be clearly observed.

The magnetic susceptibility $\chi(T)$ above $T_N \approx 20$ K agrees with the Curie-Weiss law $\chi = \chi_0 + C/(T - \Theta_{\text{CW}})$, where χ_0 is the contribution from diamagnetism and Van Vleck paramagnetism, C is the Curie constant, and Θ_{CW} is the Curie-Weiss temperature [56]. Fitting the data between 75 and 300 K yields $\chi_0 = -6.5(5) \times 10^{-4}$ emu $\text{Oe}^{-1} \text{mol}^{-1}$, $C = 4.38(3)$ emu K mol^{-1} , and $\Theta_{\text{CW}} = -168(2)$ K. The negative Curie-Weiss temperature indicates that the dominant exchange interaction of $\text{Ba}_2\text{MnTeO}_6$ is antiferromagnetic. The effective moment is estimated to be $\mu_{\text{eff}} = 5.88(1) \mu_B$, close to the theoretical effective moment $\mu_{\text{eff}} = g\sqrt{S(S+1)} = 5.91 \mu_B$ for the high spin configuration of Mn^{2+} with $S = 5/2$. The magnetic susceptibility $\chi(T)$ of the Mn_3O_4 impurity was not considered due to the low Mn_3O_4 content and the weak $\chi(T)$ for paramagnetic Mn_3O_4 [57].

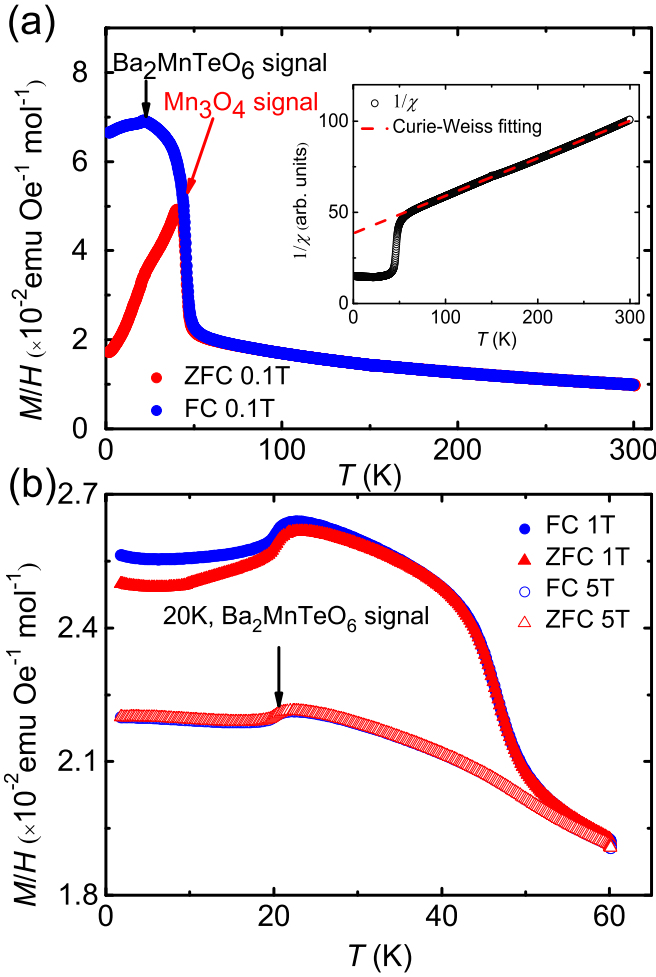


FIG. 4. (a) FC and ZFC magnetic susceptibility measured at $\mu_0 H = 0.1 \text{ T}$. The inset shows the inverse susceptibility and high-temperature Curie-Weiss fitting. (b) FC and ZFC magnetic susceptibility at $\mu_0 H = 1$ and 5 T .

V. SPECIFIC HEAT

Specific heat measurements against temperature are presented in Fig. 5(a). A sharp λ -like transition occurs at $T_N \approx 20 \text{ K}$. A modified Debye model considering the existence of two phonons that reconcile the heavy atoms (Ba, Mn, Te) and light atoms (O) was employed to describe the data from 55 to 200 K . The modified Debye model follows the formula [58]:

$$C_{ph} = 9R \sum_{n=1}^2 C_n \left(\frac{T}{\Theta_{Dn}} \right)^3 \int_0^{\Theta_{Dn}/T} \frac{x^4 e^x}{(e^x - 1)^2} dx. \quad (2)$$

The modeling indicates that, of the 10 atoms in the formula unit, 4.5 atoms have a Debye temperature Θ_{D1} of $249 \pm 4 \text{ K}$ and 5.5 atoms have a Debye temperature Θ_{D2} of $753 \pm 20 \text{ K}$, close to the ratio of 4 : 6 of the heavy atoms (Ba, Mn, Te) to the light atoms (O) in $\text{Ba}_2\text{MnTeO}_6$. The two phonon Debye model was also successfully applied in $\text{Sr}_2\text{MnTeO}_6$ [55]. The phonon contribution is extrapolated down to 1.8 K and the magnetic contribution was extracted by subtracting the phonon contribution from the total specific heat, as presented in Fig. 5(a).

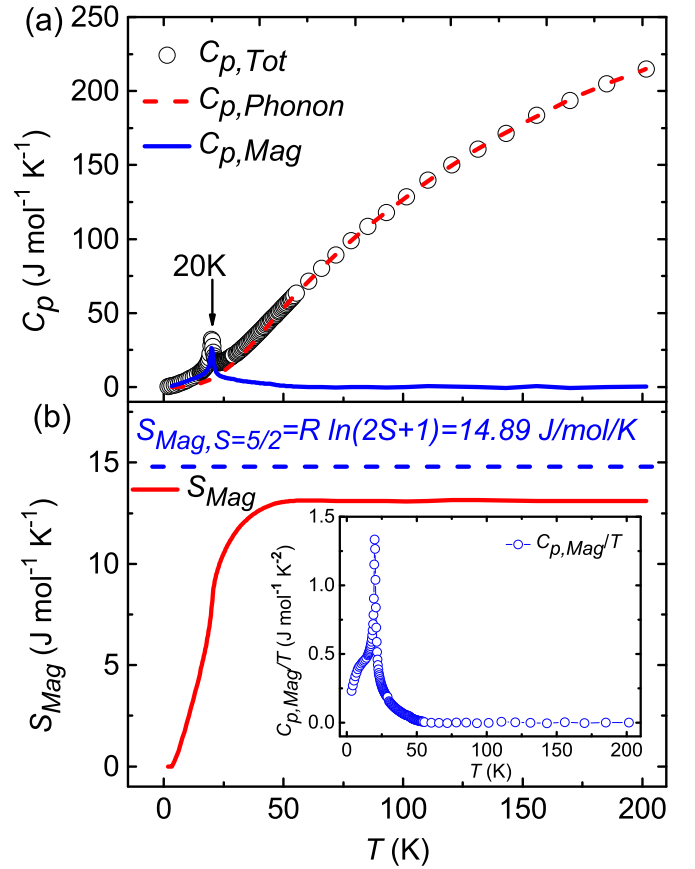


FIG. 5. (a) Specific heat C_p measured at zero magnetic field. The red dashed line is the phonon contribution fitted using a modified Debye model. The blue solid line represents the magnetic contribution. (b) The red solid line is the magnetic entropy S_{mag} and the blue dashed line marks the expected magnetic entropy for Mn^{2+} with $S = 5/2$. The inset shows the magnetic contribution of the heat capacity divided by T , $C_{p,mag}/T$.

The magnetic entropy $S_{mag} = \int C_{p,mag}/T dT$ is attributed to the magnetic state change, yielding $S_{mag} = 13.11 \text{ J mol}^{-1} \text{K}^{-1}$ at 200 K , as shown in Fig. 5(b). This value is close to the theoretically expected value for $S = 5/2$, where $S_{mag} = R \ln(2S+1) = 14.89 \text{ J mol}^{-1} \text{K}^{-1}$. The reduction of S_{mag} could arise from magnetic frustration and covalency of $3d$ electrons of Mn^{2+} with the $2p$ electron of O^{2-} , consistent with the reduced ordered moment obtained from the NPD data.

VI. MAGNETIC EXCITATIONS

Figures 6(a) and 6(b) show the INS data collected at 1.5 K with incident energies of $E_i = 14.8$ and 3.7 meV , respectively. The excitations exhibit clear dispersions, with intensities decreasing with increasing $|Q|$, demonstrating a magnetic origin. Magnetic excitations at $|Q| = 0.77, 1.09, 1.72,$ and 1.88 \AA^{-1} correspond to the magnetic Bragg peaks $(H, K, L) = (0.5, -0.5, 1), (0.5, 0.5, 0), (0.5, 0.5, 3),$ and $(0.5, -0.5, 4)$, respectively. No spin gap is observed in either spectrum, possibly because of the instrumental limitation or its gapless nature. For a further understanding of the powder

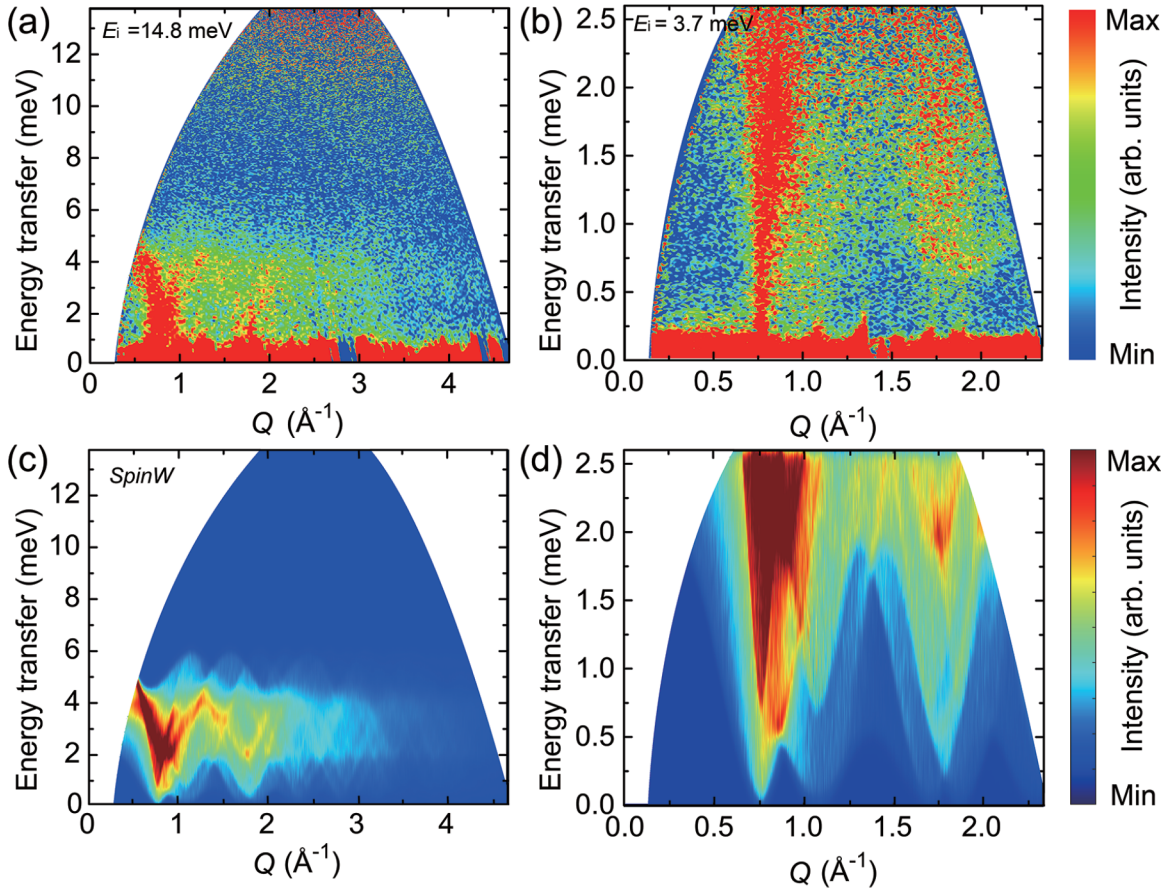


FIG. 6. INS data measured with incident neutron energies of (a) $E_i = 14.8$ and (b) 3.7 meV at $T = 1.5$ K. [(c) and (d)] Simulated powder-averaged INS data using SPINW with $J_1 = 0.27$ meV, $J_2 = 0.27$ meV, $J_3 = -0.05$ meV, and $D_{zz} = -0.01$ meV. The instrument resolution (c) $\Delta E = 0.35$ and (d) 0.14 meV are convoluted. The magnitude of intensity is shown in color. The red color represents the maximum intensity and the blue color represents the minimum intensity.

averaged spectrum, we turn to linear spin wave theory using the SPINW package.

The simulation considered the exchange couplings J_1 , J_2 , J_3 , and an easy-axis anisotropy D_{zz} . The constructed Hamiltonian was

$$\hat{H} = \sum_{i,j} J_{i,j} \mathbf{S}_i \cdot \mathbf{S}_j + D_{zz} \sum_{i,z} S_{i,z}^2, \quad (3)$$

where $J_{i,j}$ denotes the exchange coupling parameters, as shown in Fig. 1(c). The second term is the easy-axis anisotropy, which would lead to a spin gap and determines the spin directions. We note that the component of the spin operator in the rotated local frame is $S_{i,z}$, whose z axis is along the direction of the classical spin S_i [59].

A significant contribution from the MDDI is expected to be a driving force in determining the direction of the magnetic moments in $\text{Ba}_2\text{MnTeO}_6$. We employ a small value of $D_{zz} = -0.01$ meV as the easy-axis anisotropy term for $\text{Mn}_4\text{Ta}_2\text{O}_9$ in the simulation [50]. The NN intralayer coupling J_1 with Mn-Mn distance $5.7533(6)$ Å and the NN interlayer coupling J_2 with Mn-Mn distance $5.7566(6)$ Å occur through $\text{Mn}^{2+}\text{-O}^{2-}\text{-O}^{2-}\text{-Mn}^{2+}$ and $\text{Mn}^{2+}\text{-O}^{2-}\text{-Te}^{6+}\text{-O}^{2-}\text{-Mn}^{2+}$ superexchange paths as shown in Fig. 1(a). According to the Goodenough-Kanamori rule, the coupling through the former path is antiferromagnetic [60]. The latter coupling is nearly

90° , as shown in Table I, which should also be antiferromagnetic as the filled outermost orbital is the $4d$ orbital of Te^{6+} ions in other compounds with similar paths [10,11,61–63]. Therefore both J_1 and J_2 should be AF with comparable coupling strengths. The NNN interlayer coupling J_3 is also considered and corresponds to the superexchange path of $\text{Mn}^{2+}\text{-O}^{2-}\text{-Te}^{6+}\text{-O}^{2-}\text{-Mn}^{2+}$ and the Mn-Mn distance of $8.1387(7)$ Å as illustrated in Fig. 1(a). The J_3 could be either antiferromagnetic as in $\text{Sr}_2\text{CuTeO}_6$ [62] or ferromagnetic as in $\text{Sr}_2\text{MnTeO}_6$ [55].

Comparison with the experimental data allowed determination of the strengths of the exchange couplings $J_1 = 0.27(3)$ meV, $J_2 = 0.27(3)$ meV, $J_3 = -0.05(1)$ meV, and $D_{zz} = -0.01$ meV. The uncertainties of the exchange couplings are estimated by trial and error, yielding 10% uncertainty for the largest energy transfer of the acoustic branch stemming from $|Q| = 0.77$ Å⁻¹. The reproduced spectra are presented in Figs. 6(b) and 6(d), respectively. The powder INS spectra were well described by the set of exchange couplings. A spin gap around $E = 0.05$ meV emerges that is beyond the instrumental resolution. We plot the dispersion relations based on couplings along the high symmetry directions in the 3D Brillouin zone, as displayed in Fig 7. This plot would be useful to compare with spin waves measured for single-crystal samples.

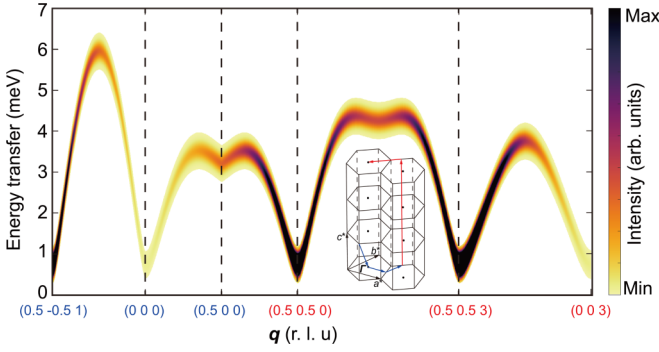


FIG. 7. Simulated spin waves along the high symmetry directions illustrated as blue and red paths in the three dimensional Brillouin zone as shown in the inset. Intensities are represented by color.

VII. MAGNETIC PHASE DIAGRAM

To quantify the effect of these exchange couplings in stabilizing the magnetic ground state of $\text{Ba}_2\text{MnTeO}_6$ and materials with similar structure, a magnetic phase diagram is derived by considering the exchange couplings J_1 , J_2 , and J_3 based on a pure Heisenberg model without considering the D_{zz} . We assume $J_1 > 0$, $J_2 > 0$, and that the sign of J_3 is variable, and define $\alpha = J_2/J_1$, $\beta = J_3/J_1$ for visualization. Here, we consider a magnetic ground state for the system with a single propagation vector \mathbf{q} defined as

$$\mathbf{q} = q_a \mathbf{a}^* + q_b \mathbf{b}^* + q_c \mathbf{c}^*, \quad (4)$$

where \mathbf{a}^* , \mathbf{b}^* , and \mathbf{c}^* are the reciprocal space basis vectors corresponding to basis vectors \mathbf{a} , \mathbf{b} , and \mathbf{c} in real space as

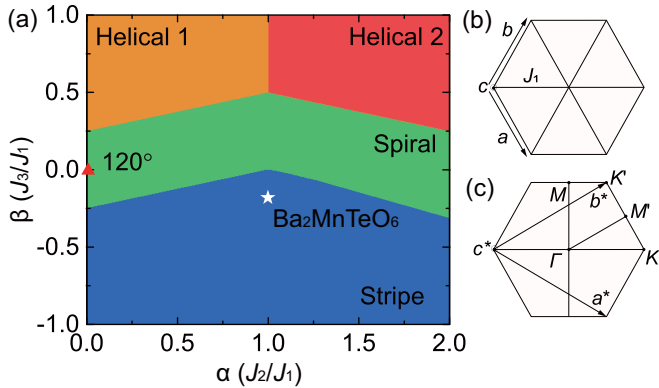


FIG. 8. (a) A magnetic phase diagram with variable exchange couplings for structures similar to $\text{Ba}_2\text{MnTeO}_6$. The helical 1 and helical 2 phases represent magnetic structures with propagation vectors $\mathbf{q}_1 = (-0.5, 0.5, 1/2)$ and $\mathbf{q}_2 = (0, 1, 1/2)$, respectively. The spiral phase refers to an incommensurate magnetic ordering. The stripe phase has the propagation vector $\mathbf{q}_3 = (0.5, 0.5, 0)$ with a stripe-type AF ordering. The \star in the stripe phase shows the position of $\text{Ba}_2\text{MnTeO}_6$, and the filled Δ indicates triangular layered materials with weak interlayer couplings. (b) Sketch of the triangular lattice. The lattice basis vectors are denoted \mathbf{a} , \mathbf{b} , and \mathbf{c} . J_1 refers to the NN intralayer coupling. (c) The first Brillouin zone for the triangular lattice. \mathbf{a}^* , \mathbf{b}^* , and \mathbf{c}^* refer to the basis vectors.

shown in Figs. 8 (b) and 8(c). Coordinates correspond to the crystal structure of $\text{Ba}_2\text{MnTeO}_6$ in Fig. 1(a).

The ground state of a classical spin system only contains components from S_z , and thus the product of \mathbf{S}_i and \mathbf{S}_j is given by

$$\mathbf{S}_i \cdot \mathbf{S}_j = S^2 \cos \mathbf{q} \cdot (\mathbf{r}_i - \mathbf{r}_j), \quad (5)$$

where S represents the value of the spin vector \mathbf{S} .

By combining Eqs. (3)–(5), the ground state energy E_0 is obtained as a function of q_a , q_b , q_c , α , and β :

$$\begin{aligned} \frac{E_0}{3J_1NS^2} &= 2 \cos(\pi(q_a + q_b)) \cos(\pi(q_b - q_a)) \\ &+ \cos(2\pi(q_a + q_b)) + 2\alpha \cos(\pi(q_a + q_b)) \\ &\times \cos(2\pi((q_b - q_a)/6 - q_c/3)) \\ &+ \alpha \cos(2\pi((q_b - q_a)/2 + q_c/3)) \\ &+ \beta \cos(2\pi(2(q_b - q_a)/3 - q_c/3)) \\ &+ 2\beta \cos(2\pi(q_a + q_b)) \\ &\times \cos(2\pi((q_b - q_a)/3 - q_c/3)). \end{aligned} \quad (6)$$

In Fig. 8(a), numerical analysis is employed to obtain \mathbf{q} values within the first Brillouin zone and $0 \leq \alpha \leq 2$ and $-1 \leq \beta \leq 1$ to determine the ground state with minimum E_0 [47,64,65]. Four phases are identified as presented. The stripe, helical 1, and helical 2 phases have propagation vectors $\mathbf{q} = (0.5, 0.5, 0)$, $(-0.5, 0.5, 1/2)$, and $(0, 1, 1/2)$, respectively. The spiral phase exhibits a noncollinear incommensurate order. For the helical 1 phase where J_3 is antiferromagnetic and $0 < J_2 \leq J_1$, the in-plane AF coupling J_1 dominates, resulting in AF in-plane order. When the intralayer AF coupling J_2 is strong, the magnetic order aligns ferromagnetically in-plane in the helical 2 phase. When both the interlayer couplings J_2 and J_3 are weak ($\alpha \approx \beta \approx 0$), the magnetic structure stabilizes with a 120° angle between the moments, corresponding to the propagation vector $\mathbf{q} = (1/3, 1/3, 0)$. An additional FM J_3 would drive the magnetic ground state to a collinear stripe-type AF order. $\text{Ba}_2\text{MnTeO}_6$ with values of $\alpha = J_2/J_1 \approx 1.0$, $\beta = J_3/J_1 \approx -0.18$ is within the stripe phase marked in Fig. 8(a).

VIII. DFT CALCULATION

Figure 9 show the total DOS and partial DOS of Mn $3d$ bands calculated using the LSDA and LSDA+ U (FLL)+(J) methods, respectively. The complete occupation of the majority spin is consistent with the $3d^5$ electron configuration in the high spin state $S = 5/2$ of Mn^{2+} . Bonding to antibonding splitting is visible as marked by arrows in Figs. 9(b) and 9(c). Antibonding bands are further split into the $e_g(d_{z^2}, d_{x^2-y^2})$ and $t_{2g}(d_{xy}, d_{xz}, d_{yz})$ manifolds owing to crystal splitting which is visible clearly in LSDA, but with no gap between them due to the strong Hund's coupling. Upon the addition of an orbital-dependent correction to the on-site coulomb repulsion using the LSDA+ U (FLL)+(J) method where we only consider the fully localized limit with typical values for U (3.81 eV=0.28 Ry) and J (0.75 eV=0.055 Ry) taken from Ref. [66], the band gap increases and the d -band states become smeared. Here, J accounts for the already considered repulsion between

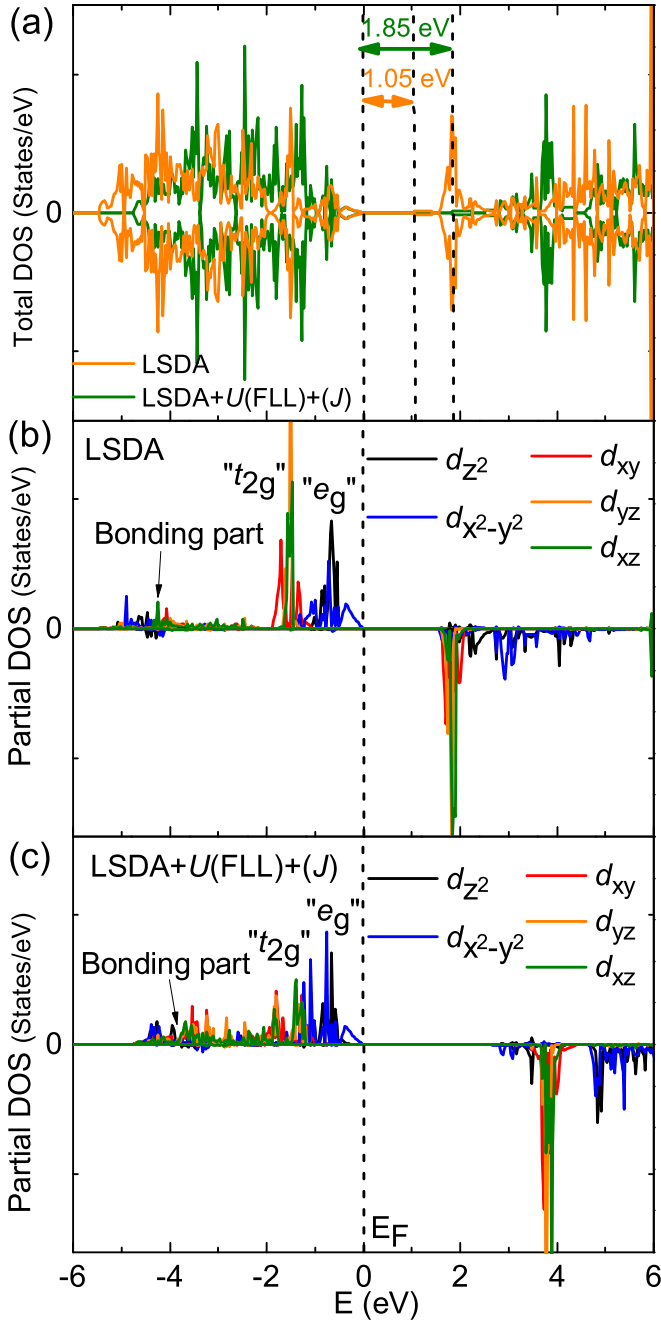


FIG. 9. (a) Total density of states (DOS) of $\text{Ba}_2\text{MnTeO}_6$. Partial d -band DOS of Mn^{2+} calculated with (b) LSDA and (c) LSDA+ $U(\text{FLL})+J$. e_g and t_{2g} represent the sum of (d_{z^2} , $d_{x^2-y^2}$) and (d_{xy} , d_{xz} , d_{yz}) bands, respectively.

the parallel spins due to the Pauli principle. Adding U shifts the occupied spin-up d bands (both e_g and t_{2g}) by $-(U - J)/2$ and the unoccupied spin-down d bands by $+(U - J)/2$.

Calculated spin moments using LSDA and LSDA+ $U(\text{FLL})+J$ are $4.27 \mu_B/\text{Mn}^{2+}$ and $4.43 \mu_B/\text{Mn}^{2+}$, respectively. The difference to the $5 \mu_B/\text{Mn}^{2+}$ comes from covalency, mainly attributed to hybridization with the $2p$ orbitals of O^{2-} . The ordered magnetic moment size calculated using LSDA+ $U(\text{FLL})+J$ is in good agreement with the NPD result of $4.49(5) \mu_B/\text{Mn}^{2+}$, indicating a

strong electron-electron repulsion correction in the system and a small orbital moment. The latter is an indicator of weak spin-orbit coupling in this compound and that the magnetic anisotropy is dominated by the MDDI with a small contribution from SOC. For the total DOS as shown in Fig. 9, the band gap using LSDA increases from 1.05 to 1.85 eV upon using LSDA+ $U(\text{FLL})+J$. The increase is due to the electron-electron repulsion correction which demonstrates that $\text{Ba}_2\text{MnTeO}_6$ could be classified as a Mott insulator.

IX. DISCUSSION AND CONCLUSION

Many two-dimensional magnetic materials such as $\text{Ba}_8\text{MnNb}_6\text{O}_{24}$ [7], $\text{Rb}_4\text{Mn}(\text{MoO}_4)_3$ [8], $\text{Ba}_3\text{MnSb}_2\text{O}_9$ [9], and $\text{Ba}_2\text{La}_2\text{MTe}_2\text{O}_{12}$ ($M=\text{Co}, \text{Ni}$) [10,11] with weak inter-layer couplings ($\alpha \approx \beta \approx 0$) show a coplanar 120° magnetic order in the spiral phase. For three-dimensional $\text{Ba}_2\text{MnTeO}_6$ with the same interlayer and intralayer exchange couplings, the frustrated parameter obtained from the estimation of an empirical formula $f = |\Theta_{\text{CW}}|/T_N$ is 8.43, which is lower than that of a strongly frustrated system with $f \geq 10$ [4]. Magnetic ordering is commonly observed in geometrically frustrated magnetic materials with large moments and high spin. In $\text{Ba}_2\text{MnTeO}_6$, the MDDI and FM NNN J_3 play crucial roles in stabilizing a stripe-type AF order. The strong electron-electron repulsion correction drives $\text{Ba}_2\text{MnTeO}_6$ to be a Mott insulator.

In summary, we carried out susceptibility, specific heat, and neutron scattering experiments to investigate the magnetic properties of the staggered stacked triangular lattice $\text{Ba}_2\text{MnTeO}_6$. A stripe-type AF order with a Néel temperature of $T_N \approx 20$ K and a propagation vector $\mathbf{k} = (0.5, 0.5, 0)$ is revealed. The spin wave excitations of the stripe AF order with energy transfer extending to 5 meV are observed at 1.5 K. Through modeling of the spin wave excitations based on linear spin wave theory, we determined the magnetic interactions $J_1 = 0.27(3)$ meV, $J_2 = 0.27(3)$ meV, $J_3 = -0.05(1)$ meV, and an easy-axis anisotropy term $D_{zz} = -0.01$ meV. The resultant couplings present within the stripe phase in the magnetic phase diagram for the triangular lattice that we derive. A FM interaction of J_3 is the key to stabilizing the collinear stripe-type AF order.

Note added. Recently, we became aware of a recent preprint posted by Mustonen *et al.* with similar experimental observations on the same compound [45]. Mustonen *et al.* describe the structure of $\text{Ba}_2\text{MnTeO}_6$ with a cubic space group $Fm\bar{3}m$ instead of the trigonal space group $R\bar{3}m$. The two structure models are close in describing $\text{Ba}_2\text{MnTeO}_6$ when we convert one space group to the other one. The $R\bar{3}m$ space group allows an additional degree of freedom for the positions of Ba and O sites along the c axis. Meanwhile, the directions of the antiferromagnetically ordered moments refined using the two models show a difference of 27° .

ACKNOWLEDGMENTS

The work is supported by the National Natural Science Foundation of China (Grants No. 11904414 and No.

11904416), Natural Science Foundation of Guangdong (Grant No. 2018A030313055), National Key Research and Development Program of China (Grant No. 2019YFA0705700), the Fundamental Research Funds for the Central Universities (Grant No. 18lgy73), the Hundreds of Talents

program of Sun Yat-Sen University, and Young Zhujiang Scholar program. S.J. and D.X.Y. are supported by NKRDPC-2018YFA0306001, NKRDPC-2017YFA0206203, NSFC-11974432, GBABRF-2019A1515011337, and Leading Talent Program of Guangdong Special Projects.

- [1] A. P. Ramirez, *Annu. Rev. Mater. Sci.* **24**, 453 (1994).
- [2] J. E. Greedan, *J. Mater. Chem.* **11**, 37 (2001).
- [3] L. Balents, *Nature (London)* **464**, 199 (2010).
- [4] L. Savary and L. Balents, *Rep. Prog. Phys.* **80**, 016502 (2017).
- [5] A. V. Chubokov and D. I. Golosov, *J. Phys.: Condens. Matter* **3**, 69 (1991).
- [6] L. Seabra, T. Momoi, P. Sindzingre, and N. Shannon, *Phys. Rev. B* **84**, 214418 (2011).
- [7] R. Rawl, L. Ge, Z. Lu, Z. Evenson, C. R. Dela Cruz, Q. Huang, M. Lee, E. S. Choi, M. Mourigal, H. D. Zhou *et al.*, *Phys. Rev. Mater.* **3**, 054412 (2019).
- [8] R. Ishii, S. Tanaka, K. Onuma, Y. Nambu, M. Tokunaga, T. Sakakibara, N. Kawashima, Y. Maeno, C. Broholm, D. P. Gautreaux *et al.*, *Europhys. Lett.* **94**, 17001 (2011).
- [9] Y. Doi, Y. Hinatsu, and K. Ohoyama, *J. Phys.: Condens. Matter* **16**, 8923 (2004).
- [10] Y. Kojima, M. Watanabe, N. Kurita, H. Tanaka, A. Matsuo, K. Kindo, and M. Avdeev, *Phys. Rev. B* **98**, 174406 (2018).
- [11] M. Saito, M. Watanabe, N. Kurita, A. Matsuo, K. Kindo, M. Avdeev, H. O. Jeschke, and H. Tanaka, *Phys. Rev. B* **100**, 064417 (2019).
- [12] M. F. Collins and O. A. Petrenko, *Can. J. Phys.* **75**, 605 (1997).
- [13] H. Kadowaki, H. Kikuchi, and Y. Ajiro, *J. Phys.: Condens. Matter* **2**, 4485 (1990).
- [14] M. Poienar, F. Damay, C. Martin, V. Hardy, A. Maignan, and G. André, *Phys. Rev. B* **79**, 014412 (2009).
- [15] M. Poienar, F. Damay, C. Martin, J. Robert, and S. Petit, *Phys. Rev. B* **81**, 104411 (2010).
- [16] S. Mitsuda, H. Yoshizawa, N. Yaguchi, and M. Mekata, *J. Phys. Soc. Jpn.* **60**, 1885 (1991).
- [17] F. Ye, J. A. Fernandez-Baca, R. S. Fishman, Y. Ren, H. J. Kang, Y. Qiu, and T. Kimura, *Phys. Rev. Lett.* **99**, 157201 (2007).
- [18] E. Wawrzyńska, R. Coldea, E. M. Wheeler, I. I. Mazin, M. D. Johannes, T. Sörgel, M. Jansen, R. M. Ibberson, and P. G. Radaelli, *Phys. Rev. Lett.* **99**, 157204 (2007).
- [19] E. Wawrzyńska, R. Coldea, E. M. Wheeler, T. Sörgel, M. Jansen, R. M. Ibberson, P. G. Radaelli, and M. M. Koza, *Phys. Rev. B* **77**, 094439 (2008).
- [20] E. M. Wheeler, R. Coldea, E. Wawrzyńska, T. Sörgel, M. Jansen, M. M. Koza, J. Taylor, P. Adroguer, and N. Shannon, *Phys. Rev. B* **79**, 104421 (2009).
- [21] L. Wulff, B. Wedel, and H. Müller-Buschbaum, *Z. Naturforsch* **53**, 49 (1998).
- [22] S. A. Ivanov, P. Nordblad, R. Mathieu, R. Tellgren, and C. Ritter, *Dalton Trans.* **39**, 5490 (2010).
- [23] P. Chanlert, N. Kurita, H. Tanaka, D. Goto, A. Matsuo, and K. Kindo, *Phys. Rev. B* **93**, 094420 (2016).
- [24] P. Chanlert, N. Kurita, H. Tanaka, M. Kimata, and H. Nojiri, *Phys. Rev. B* **96**, 064419 (2017).
- [25] C. Lacroix, P. Mendels, and F. Mila, *Introduction to Frustrated Magnetism*, Springer Series in Solid-State Sciences (Springer, Berlin, Heidelberg, 2011), Vol. 164.
- [26] S. Nakatsuji, H. Tonomura, K. Onuma, Y. Nambu, O. Sakai, Y. Maeno, R. T. Macaluso, and J. Y. Chan, *Phys. Rev. Lett.* **99**, 157203 (2007).
- [27] D. E. MacLaughlin, Y. Nambu, S. Nakatsuji, R. H. Heffner, L. Shu, O. O. Bernal, and K. Ishida, *Phys. Rev. B* **78**, 220403(R) (2008).
- [28] S. Nakatsuji, Y. Nambu, and S. Onoda, *J. Phys. Soc. Jpn.* **79**, 011003 (2010).
- [29] R. M. Morra, W. J. L. Buyers, R. L. Armstrong, and K. Hirakawa, *Phys. Rev. B* **38**, 543 (1988).
- [30] Z. Tun, W. J. L. Buyers, R. L. Armstrong, K. Hirakawa, and B. Briat, *Phys. Rev. B* **42**, 4677 (1990).
- [31] K. Kakurai, M. Steiner, R. Pynn, and J. K. Kjems, *J. Phys.: Condens. Matter* **3**, 715 (1991).
- [32] I. A. Zaliznyak, S. H. Lee, and S. V. Petrov, *Phys. Rev. Lett.* **87**, 017202 (2001).
- [33] B. Schwarz, D. Kraft, R. Theissmann, and H. Ehrenberg, *J. Mag. Mag. Mater.* **322**, L1 (2010).
- [34] A. J. Studer, M. E. Hagen, and T. J. Noakes, *Physica B* **385–386**, 1013 (2006).
- [35] H. M. Rietveld, *J. Appl. Cryst.* **2**, 65 (1969).
- [36] J. Rodríguez-Carvajal, *Physica B* **192**, 55 (1993).
- [37] D. Yu, R. Mole, T. Noakes, S. Kennedy, and R. Robinson, *J. Phys. Soc. Jpn.* **82**, SA027 (2013).
- [38] D. Richard, M. Ferrand, and G. J. Kearley, *J. Neutron Res.* **4**, 33 (1996).
- [39] S. Toth and B. Lake, *J. Phys. Condens. Matter* **27**, 166002 (2015).
- [40] K. Schwarz, P. Blaha, and G.K.H. Madsen, *Comput. Phys. Commun.* **147**, 71 (2002).
- [41] J. P. Perdew and Y. Wang, *Phys. Rev. B* **98**, 079904(E) (2018).
- [42] M. T. Czyżyk and G. A. Sawatzky, *Phys. Rev. B* **49**, 14211 (1994).
- [43] M. Rotter, *J. Magn. Mag. Mat.* **272–276**, E481 (2004).
- [44] M. Rotter, M. Loewenhaupt, M. Doerr, A. Lindbaum, H. Sassik, K. Ziebeck, and B. Beuneu, *Phys. Rev. B* **68**, 144418 (2003).
- [45] O. H. J. Mustonen, C. E. Pughe, H. C. Walker, H. M. Mutch, G. B. G. Stenning, F. C. Coomer, and E. J. Cussen, *Chem. Mater.* **32**, 7070 (2020).
- [46] S. Vasala and M. Karppinen, *Prog. Solid State Chem.* **43**, 1 (2015).
- [47] S. Asai, M. Soda, K. Kasatani, T. Ono, M. Avdeev, and T. Masuda, *Phys. Rev. B* **93**, 024412 (2016).
- [48] E. F. Bertaut, *J. Appl. Phys. Suppl.* **33**, 1138 (1962).
- [49] E. F. Bertaut, *J. Phys. Colloques* **32**, C1-462 (1971).
- [50] N. Narayanan, A. Senyshyn, D. Mikhailova, T. Faske, T. Lu, Z. Liu, B. Weise, H. Ehrenberg, R. A. Mole, W. D. Hutchison *et al.*, *Phys. Rev. B* **98**, 134438 (2018).
- [51] D. C. Johnston, *Phys. Rev. B* **93**, 014421 (2016).
- [52] G. B. Jensen and V. Nielsen, *J. Phys. C: Solid State Phys.* **7**, 409 (1974).

- [53] B. Chardon and F. Vigneron, *J. Magn. Magn. Mater.* **58**, 128 (1986).
- [54] R. J. Goff, A. J. Williams, and J. P. Attfield, *Phys. Rev. B* **70**, 014426 (2004).
- [55] L. Ortega-San Martin, J. P. Chapman, L. Lezama, J. Sánchez Marcos, J. Rodríguez-Fernández, M. I. Arriortua, and T. Rojo, *Eur. J. Inorg. Chem.* 1362 (2006).
- [56] S. Blundell, *Magnetism in Condensed Matter* (Oxford University Press, 2001), Vol. 1.
- [57] R. Tackett, G. Lawes, B. C. Melot, M. Grossman, E. S. Toberer, and R. Seshadri, *Phys. Rev. B* **76**, 024409 (2007).
- [58] N. Ahmed, A. A. Tsirlin, and R. Nath, *Phys. Rev. B* **91**, 214413 (2015).
- [59] A. V. Chubukov, S. Sachdev, and T. Senthil, *J. Phys.: Condens. Matter* **6**, 8891 (1994).
- [60] J. Kanamori, *J. Phys. Chem. Solids* **10**, 87 (1959).
- [61] K. Yokota, N. Kurita, and H. Tanaka, *Phys. Rev. B* **90**, 014403 (2014).
- [62] T. Koga, N. Kurita, M. Avdeev, S. Danilkin, T. J. Sato, and H. Tanaka, *Phys. Rev. B* **93**, 054426 (2016).
- [63] R. Rawl, M. Lee, E. S. Choi, G. Li, K. W. Chen, R. Baumbach, C. R. dela Cruz, J. Ma, and H. D. Zhou, *Phys. Rev. B* **95**, 174438 (2017).
- [64] S. Asai, M. Soda, K. Kasatani, T. Ono, V. O. Garlea, B. Winn, and T. Masuda, *Phys. Rev. B* **96**, 104414 (2017).
- [65] S. Jin, C. Luo, T. Datta, and D. X. Yao, *Phys. Rev. B* **100**, 054410 (2019).
- [66] I. V. Solovyev, P. H. Dederichs, and V. I. Anisimov, *Phys. Rev. B* **50**, 16861 (1994).